

Supplementary Materials for  
**Fluid dynamical pathways of airborne transmission while waiting in a line**

Ruixi Lou *et al.*

Corresponding author: Varghese Mathai, [vmathai@umass.edu](mailto:vmathai@umass.edu)

*Sci. Adv.* **11**, eadw0985 (2025)  
DOI: 10.1126/sciadv.adw0985

**The PDF file includes:**

Supplementary Text  
Figs. S1 to S10  
Legends for movies S1 to S4

**Other Supplementary Material for this manuscript includes the following:**

Movies S1 to S4

## I. EXPERIMENTAL APPARATUS

The experimental setup made use of an Arduino micro-controller and a stepper motor controller to mimic the periodic movements in waiting line with precise control over walking and waiting cycles. The measurement section was located at the center of a  $1.8\text{ m} \times 0.46\text{ m} \times 0.46\text{ m}$  water tank with a 80/20 aluminum framing. The conveyor belt was attached to two 3D-printed pulleys and was driven by the stepper motor, which connected to the pulley to mimic the periodic motion of the waiting. A high-torque (12 Nm) Nema-34 stepper motor drove the periodic motion of the system via the Arduino micro-controller along with DM556 stepper motor driver. The program was coded in Arduino IDE and AccelStepper library is used in the program. We mounted the system on a Teflon-coated, double-U-channel system to minimize vibrations of the belt in an accelerating-decelerating system while simultaneously visualizing passive scalar transport and tracking the fluid motion.

The 3D-printed cylindrical dummies are glued to the conveyor belt to mimic people walking and waiting in a line (or queue). 3D printing was used to print dummies of a cylindrical shape whose diameter will be determined by matching the non-dimensional parameter  $A^*$  of an actual waiting line. Further, ensuring dynamic similarity, we designed the dummies to be around 2.5 cm in diameter and 11 cm in height for water as the working fluid. we use water. Two Photron Nova S-9 high speed cameras were used in the imaging experiments, one for the side view and the other one for the top view images for dye visualization and Particle Image Velocimetry (See Fig. [S-1](#))

To minimize external influences and free-surface sloshing effects, an acrylic plate was inserted just below the free surface of the water. The cylindrical dummies in the measurement section in this setup were fixed inverted under the water. Since the belt and pulleys were above the water, their movement did not generate any secondary flows in the water other than due to the motion of the dummies themselves. A syringe pump was used to inject the saline water, both in Dye illumination and PIV experiments. The density contrast with water mimics the buoyancy effect. The syringe pump was constructed by assembling 3D printed parts sliding on an 80/20 rail, with flanged sleeve bearings and a stepper motor driving a cam-shaft. The cam design, together with a porous air-stone glued to the upper quarter height of the dummy enabled a controlled injection of the fluorescent dye. The dye seeps out through a porous air-stone. This injection arrangement resembled the gentle



release of the breath plume. Pictures of the syringe pump and dye injection are shown in Fig. S-1.

For the dye illumination experiments, we used a Fluorescein Disodium Salt dye, illuminated with blue LED lights. For the Particle Image Velocimetry (PIV) experiments, the 3D-printed cylindrical dummies were replaced with hollow, fluid-filled glass cylindrical dummies to allow the laser light to pass through. The laser beam was expanded to a laser sheet using a plano-concave cylindrical lens of -20 mm focal length. Refractive index matching was performed, and density-matched polyamide microspheres were used as PIV seeding particles. The laser used was a 2W diode-pumped solid-state (DPSS) type of 532 nm wavelength. The PIV videos were processed with the PIVlab software in Matlab to generate the 2D velocity field. Side-view and top-view measurements were performed. A schematic of the raw PIV experiment is shown in Fig. S-1.

## II. DIMENSIONLESS NUMBERS

To study buoyancy effects from the breathing plumes on the flow, we define their strength using non-dimensional numbers. Instead of using temperature differences to dynamically match buoyancy effects, we directly use a density difference induced through scalar concentration. To do this, we rewrite the Grashof number in terms of the density difference:

$$Gr = \frac{g \frac{\Delta \rho}{\rho} D_c^3}{\nu^2}, \quad (1)$$

where  $\Delta \rho$  is density difference of the fluids,  $\rho$  the density of the environmental fluid (in our case, water) and  $D_c$  is the characteristic length, which is set as the diameter of cylinder.

To convert the temperature difference to the density difference for the experiments, we match the Grashof number of exhaled breath ( $Gr_a$ ) with a Grashof number from injected salt water ( $Gr$ ) in the experiments:

$$Gr = \frac{g \frac{\Delta \rho}{\rho} D_c^3}{\nu^2} = \frac{g \beta \Delta T D_s^3}{\nu_a^2} = Gr_a \quad (2)$$

which yields the relationship:

$$\Delta T = \frac{1}{\beta} \frac{\Delta \rho}{\rho} \left( \frac{D_c^3}{D_s^3} \right) \left( \frac{\nu_a^2}{\nu^2} \right) \quad (3)$$

where  $\beta$  is the thermal expansion coefficient of the fluid.

To calculate the temperature difference between human exhalation and the ambient temperature, we follow the models used in Yang *et al.* (40), Houdas and Ring (41). Taking 37°C as the human core temperature, the human periphery temperature changes in relation to the ambient temperature(Houdas and Ring (41)). The exhaled breath temperature is set as the arithmetic mean of the human periphery temperature and the ambient temperature. For example,  $\Delta\rho/\rho = 0.16$  corresponds to an ambient temperature of 22°C and a periphery temperature of 32°C. For the other limit of  $\Delta\rho/\rho = 0$ , it corresponds to the situation that the ambient temperature ( $T_a \approx 35^\circ\text{C}$ ) is equal to the periphery temperature ( $T_s \approx 35^\circ\text{C}$ ).

### III. DYE DISPERSAL FOR HUMAN-SHAPED MODELS AND CYLINDRICAL MODELS

In Fig. S-2 we show comparisons of dye transport for cylindrical models (*upper row*) and human shaped models (*lower row*) for non-buoyancy (*left column*) and buoyant settings (*right column*) after a time  $t/\tau_l = 1$ . The large-scale transport is observed to be similar for the cylindrical model case and the human-shaped models case.

### IV. EFFECT OF HUMAN BODY THERMAL PLUME

We also examined the effect of the human body thermal plume. Our experiments and DNS also suggest that the human thermal plume is restricted to a small distance of  $\sim 1\text{cm}$  from the skin-surface. Further, the strength of the body thermal plume is weak(Craven and Settles (58), Wang *et al.* (59), Salmanzadeh *et al.* (60), Bogdan *et al.* (61), Gena *et al.* (63)) compared to the kinematically-induced air currents such as the “downwash”. We can see this in Fig. S-4 a. In Fig. S-4 a(*left and right*), we compare the flow pattern with and without the body thermal effect. The overhead region of the cylinders are significantly affected by the body thermal plume, which is in agreement with observations from literature(Fig. S-3 a-b. However, importantly, the flow in the region between the cylinders is nearly unchanged by the presence of the human thermal plume. The downwash persists. In Fig. S-4 b,c we compare the effect of the the body temperature on the trajectories of the particles. The plume does not majorly change the breathe plume transport as the breath plume. This is

mainly because the release location of the breath-plume is well-outside the boundary layer of the body thermal plume. Indeed, there are some secondary effects of the body thermal plume on the aerosol transport. The human thermal plume influences the air velocities above the head of the individuals (see Fig. S-4 a region marked green outline). We also noticed that the body thermal plume has an effect of prolonging the duration of the downwash current, since the continuity condition necessitates a counter flow to the upward plume around the body.

## V. EFFECT OF PHYSICAL SEPARATION

We experimentally studied the effect of physical separation in the waiting lines by conducting experiments for 3 feet, 6 feet and 12 feet separations of waiting lines, which correspond to non-dimensional separations of  $A^* = 2.5$ ,  $A^* = 5$  and  $A^* = 10$ . We checked how the released dye evolves, and measured the velocities using PIV.

The results in this section show that physical separation plays only a minor role in the passive scalar transport, and hence that increasing the physical separation does not alleviate the problems of disease transmission in waiting lines. Fig. S-6 shows that for double the separation the scalar ends up largely in the same place, i.e. in front of the susceptible person, after a cycle of movement. Therefore, doubling the distance will do nothing to avoid contagion.

However, cylinder separation do affect the flow velocity patterns, as shown in Fig. S-6. The velocity magnitude in the  $x$ -direction (i.e. the direction of motion) within the intermediate region between two cylinders is greater when the separation is small ( $A^* = 2.5$ ) compared to when it is larger ( $A^* = 5$  and  $A^* = 10$ ), as the cylinders catch the wake of each other. There is no developed wake for  $A^* = 2.5$ , and the  $x$ -velocity magnitude in the cylinder separation region is, on average, much higher and closer to the cylinder moving speed.

## VI. EVOLUTION OF BUOYANT PLUMES

Fig. S-7 shows the time evolution of the uprising buoyancy plumes after the motion comes to stop for ambient temperatures of 22°C , 28°C and 35°C. Because of the density differences

between the exhalation plume and the surroundings, plumes rise. This upwards velocities are signified as red areas in the color plots. As expected, plumes drift upwards as time evolves; and for lower ambient temperature (higher density differences), plumes also rise higher. The difference between the buoyant case and the non-buoyant case is due to the breath plume merging with the downwash current when the plume is not buoyant.

We can model this vertical displacement by looking at the aerosols as a buoyant plume in water. For the uprising buoyancy velocity of a buoyant plume in water, we have two components of forces of opposite directions: a force upwards due to gravity and a force which resists the movement of the fluid packet.

The buoyancy uprising force is:

$$F_1 = \frac{\Delta\rho g \pi \ell_p^3}{6}, \quad (4)$$

while the downwards force can be modelled as a drag force:

$$F_2 = \frac{\rho v_r^2 \pi \ell_p^2 C_d}{8}, \quad (5)$$

where  $v_r$  is the uprising buoyancy velocity;  $\ell_p$  is the length scale of buoyant plume;  $\rho$  is the density of the fluid and  $\Delta\rho$  is the density difference between the plume and fluid.

For a constant buoyancy velocity, the net force would cancel. Setting these two forces to be equal to each other, we get:

$$v_r = \sqrt{\frac{4\Delta\rho g \ell_p}{3\rho C_d}} = \kappa \sqrt{\frac{\Delta\rho}{\rho}}, \quad (6)$$

with

$$\kappa = \sqrt{\frac{4g\ell_p}{3C_d}}, \quad (7)$$

where  $\kappa$  is the same constant used in Fig. 4d in the main paper, which was fit to DNS data. If we set  $\ell_p$  equal to the diameter of the released passive scalars (about diameter of the cylinder) and  $C_d \sim 1$ , we can estimate  $\kappa \approx 1.1\sqrt{g\ell_p}$ . In comparison, the value obtained from a fit to the DNS data for a rising thermal plume was  $\kappa \approx 0.23\sqrt{g\ell_p}$ , which was used in the model. The lower prefactor obtained in our DNS is likely due to our assumption that the buoyant blob maintains the original size scale  $\ell_p$  during its rise. Typically, turbulent thermal plumes can be expected to break up due to shear as they rise, consequently reducing its rise velocity. A prefactor of  $\approx 0.2$  has also been observed in prior works on turbulent thermal convection (Jiang *et al.* (49)).

## VII. VARIATION IN EXPULSION STRENGTH

Although the focus of the current study is strictly limited to breath-like expulsions, where aerosols are released near the face and transported by the air currents in the waiting line, we also performed a few experiments with stronger expulsions – to approximately mimic the release of aerosols during “talking” and “sneezing” type events, through incremental changes in the momentum of the released dye (See Fig. S-8 *left to right* increasing in strength of expulsion). The final location of aerosols has some changes depending on the strength of the expulsion event itself as shown in Fig. S-9 (a)-(c). The breath-like expulsion is pushed down the furthest, while the intermediate expulsion travels furthest forward. However, these differences in the location of the dye are not due to the expulsion events themselves, but rather arise due to the region of the air current where the expulsion event first releases aerosols. Notably, the breath-plume is released in the region of strongest downwash and sinks fastest. The sneeze-plume is released at a farther distance from the body, where the downwash current is weaker, and it therefore sinks less than the breath-plume. We show this using tracer particle trajectories released at a forward location where the downwash is weaker (see trajectories in Fig. S-10). Thus, the expulsion strength has a secondary effect on the transport, because the airflow where the expulsion releases aerosols can be different.

In a follow-up work, we aim to systematically explore the influence of the strength of various kinds of expulsion events and the transport of inertial droplet transport (e.g. breathing, intermittent talking, “Plosive sounds”, sneezing, and coughing) on the airborne transmission in a waiting line. We note that the scope of the present work is strictly on the transport of tiny aerosols that are typically released during normal breathing, and the risks posed by them under prolonged exposure conditions in waiting lines.

## VIII. HORIZONTAL DISPERSION

We provide a quantitative study of the mean square displacement (MSD) of the tracer particles by analyzing the difference between particles released in front of the cylinder (as an infected person would do), and those to the side and behind the person. Direct visualization of the trajectories of the Lagrangian tracers is shown in Fig. S-10a,b. We compare the non-buoyant case with the buoyant case: we observe that the trajectories of front-released

particles of both cases are similar for the first period (after release) and they move forward quickly. Quantitatively, we take the Mean horizontal dispersion into comparison (see Fig. S-10.c), observing that both cases overlap for the first circle for front release which is consistent with the high similarity between a and b of Fig. S-10. Fig. S-10.d shows the MSD of the vertical and horizontal displacement of particles released in front of the cylinder. The log-scale MSD plots of different cases do not show a significant dependency of buoyancy. To zoom into the differences, we also show linear-scale plots in insets of the figure: both the vertical MSD and the horizontal MSD differ less from case to case than that of side&rear released particles.

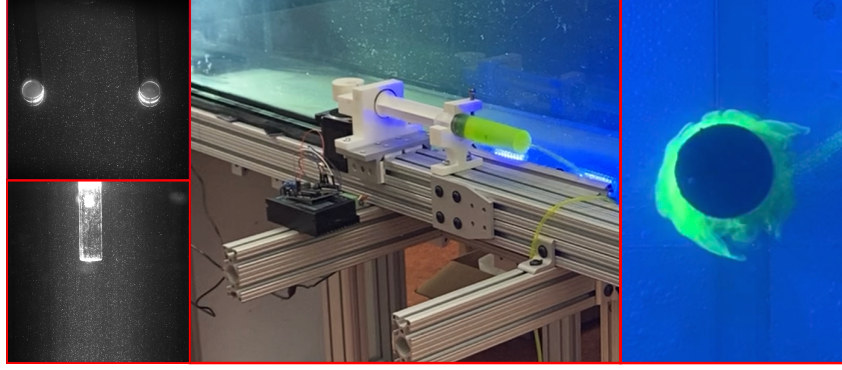


FIG. S-1. **Experimental images from PIV and dye visualization.** Sample raw images from PIV experiments of top view and side view (Left). Syringe pump used for injecting dye (Middle). Sample image of dye injection (Right).

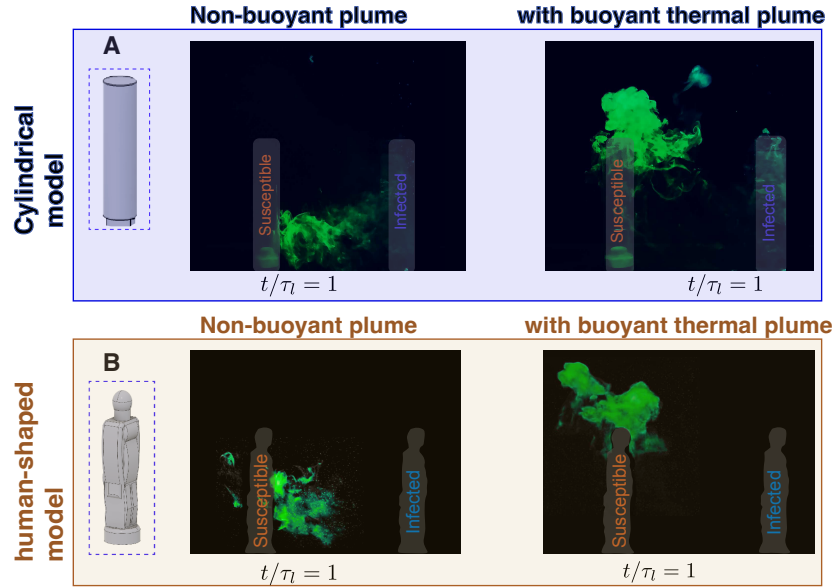


FIG. S-2. **Experimental visualization of the transported location of released (in green) dye during a walk-waiting cycle.** (a – upper row) is for cylindrical dummy and (b – lower row) is for human shaped model. The final transported location in the non-buoyant case is shown on the left column and in the buoyant thermal plume case is shown in the right column. The differences due to a change in the geometry of the model are not significant which may be due to equivalent diameter of the cylinder and human shaped dummy being similar. A downwash is observed in both cases.

Prior works showing the region of influence and strength of the human thermal plume (a), (b).

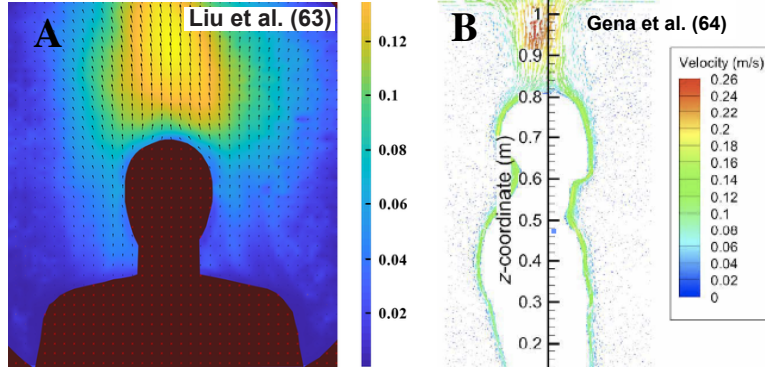


FIG. S-3. Images from prior works showing the velocity of air due to human body thermal plume. (a) and (b) show the region of influence from front view and side view around an individual(Liu *et al.* (62), Gena *et al.* (63)). The colorbar ranges show the magnitude of the velocity. The body thermal plume is low speed and its influence is localized to a distance of  $\sim 1$  cm from the skin surface (as evident from (b)), except the overhead region where the velocity is comparable to the speed of the downwash speed. The effect of the body thermal plume is further elaborated through DNS simulations shown in a later figure.



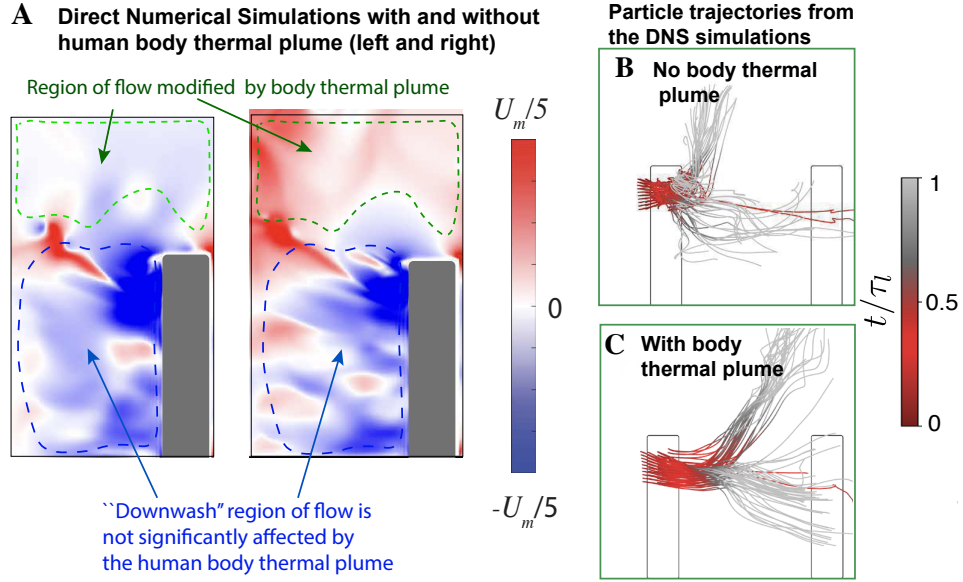


FIG. S-4. **Direct Numerical simulations (DNS) and trajectories of released particles with an without human body thermal plume modeled.** (a) DNS result of the vertical velocity field in the absence of body thermal plume (*left*), and with body thermal plume (*right*) for the high risk condition. Lagrangian trajectories of aerosols for the DNS field in the absence of human body thermal plume is shown in (b), and in the presence of body thermal plume is shown in (c). The body thermal plume does not majorly affect the vertical drift of the particle trajectories, although the rising plume is found to impart a gentle forward momentum to the aerosols. The competing effects of the downwash and the thermal buoyancy are still dominant with the body thermal plume effect included.

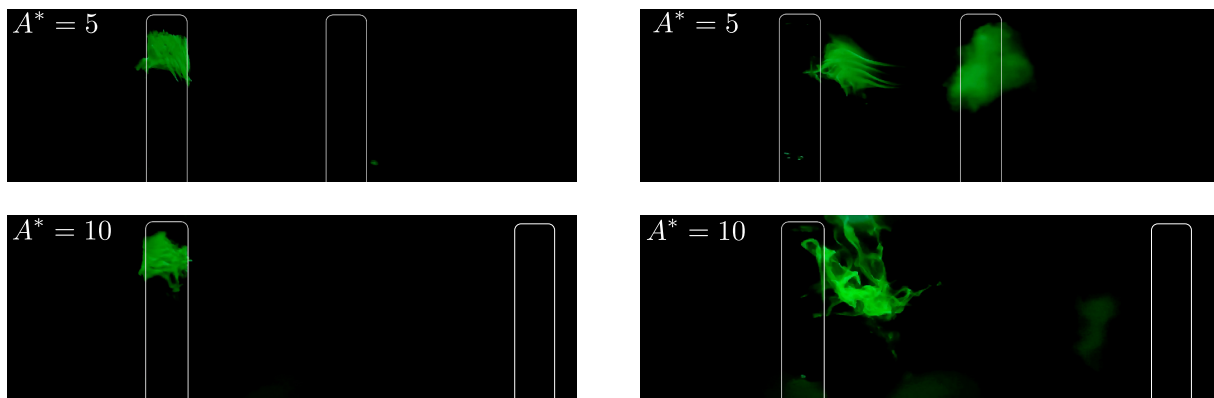


FIG. S-5. **Dye visualization for different physical separations.** Illuminated dye pattern when the motion is about to start (left) and when the motion just stops (right) for separations equal to  $A^* = 5$  (upper row) and  $A^* = 10$  (lower row). Here,  $A^* = 5$  was equivalent to a “six-feet” physical separation, and 10 m was equivalent to “twelve-feet” physical separation.

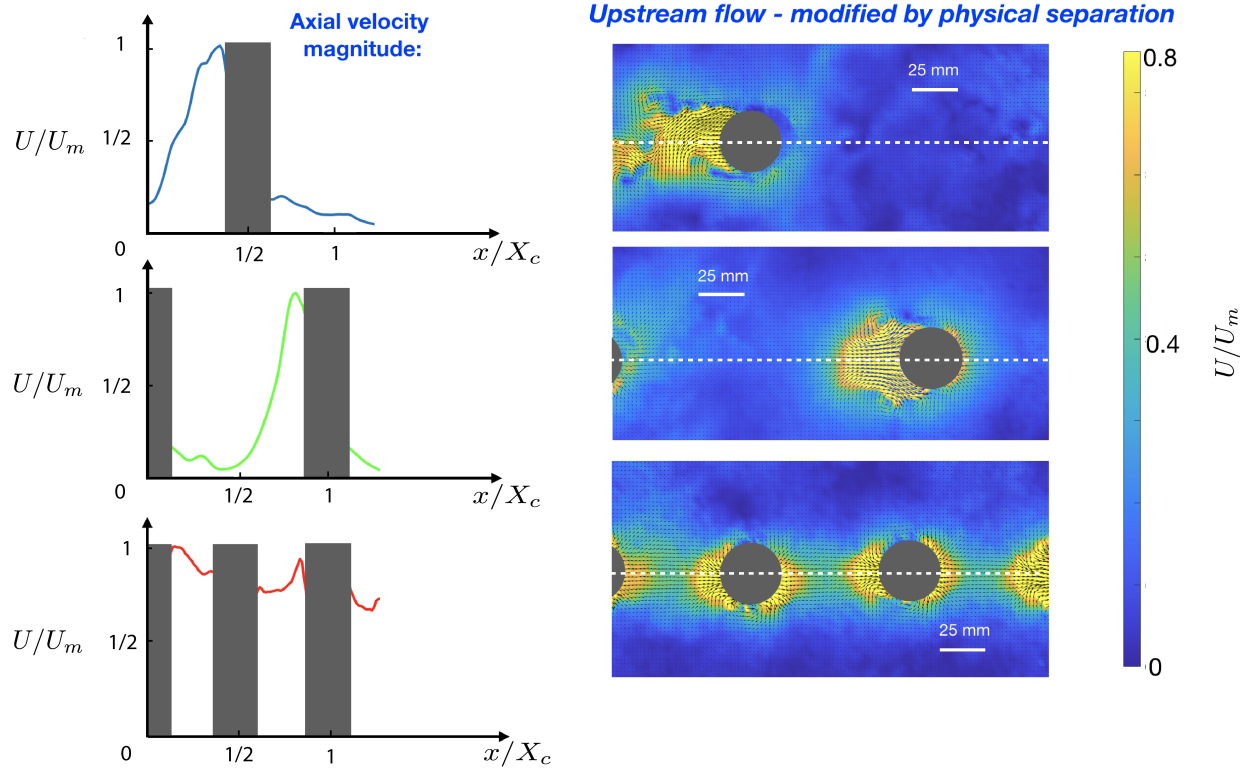


FIG. S-6. **Top-view velocity fields obtained from PIV for different physical separations.**

The left panels show the  $x$ -velocity (in the direction of motion) magnitude against the  $x$ -position along the cylinder mid-plane (indicated with a dotted line in the right panels), for non-dimensional separations of  $A^* = 10$ ,  $A^* = 5$  and  $A^* = 2.5$  from top to bottom. The grey rectangles in the plots represent the location of the cylindrical dummies. The right panels show a top-view of the velocity field for the corresponding values of non-dimensional separation. The grey circles represent the cylindrical dummies. All plots are at the time instant when the cylinders are moving and have travelled half of their separation.

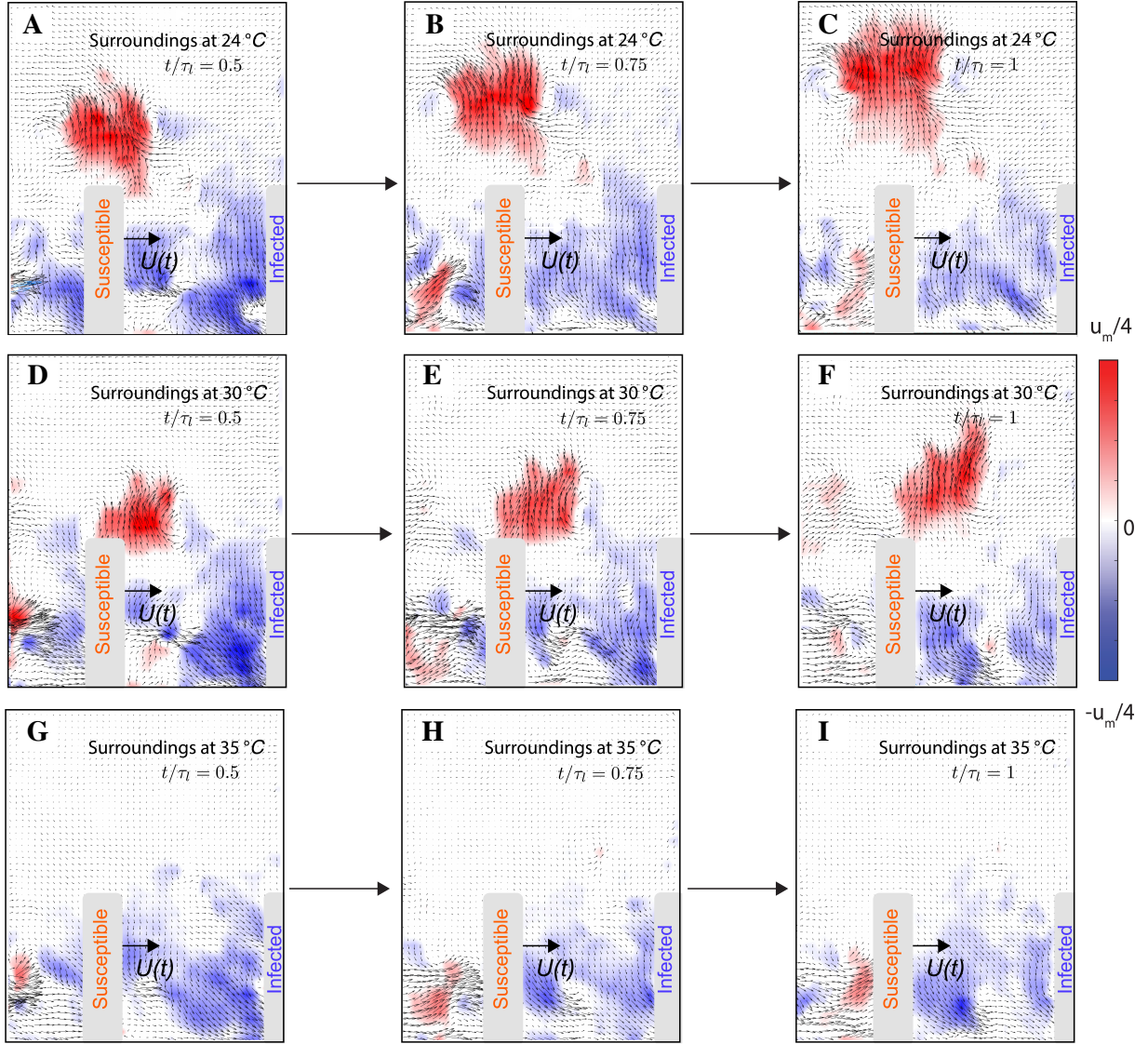


FIG. S-7. **Evolution of uprising buoyancy plumes under different ambient temperatures.** (Left to right):  $t/\tau_l = 0.5$ ,  $t/\tau_l = 0.75$  and  $t/\tau_l = 1$ . (a-c) PIV vertical velocity fields of the condition that surroundings at 22°C; (d-f) PIV vertical velocity fields of the condition that surroundings at 28° C; (g-i) PIV vertical velocity fields of the condition that surroundings at 35°C.

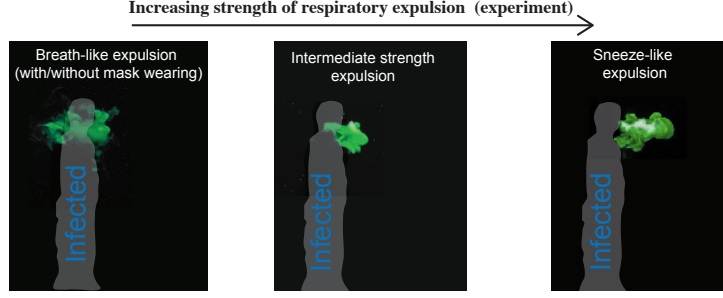


FIG. S-8. **Experiments showing plume expulsions of different strengths.** Left to right shows experiments performed with human-shaped models to mimic breath-like, talking, and sneeze-like expulsions.

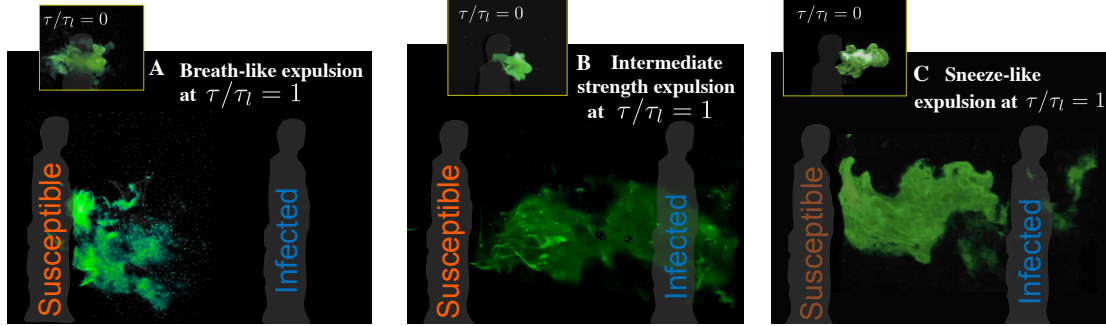


FIG. S-9. **Experiments showing plume transport after one walking cycle, for expulsions of different strengths.** (a)-(c) Transported locations of the dye for the different strengths of expulsions shown earlier in Fig. [S-8](#). Here, (a) shows the transported locations of dye corresponding to a breath-like expulsion, (b) shows the transport of an intermediate strength expulsion, and (c) mimics a sneeze-like expulsion event. These three expulsions affect the initial release of the aerosols, at which the downwash current differs in its strength. The spatial difference in the underlying flow can account for the observed differences in the transport in (a)-(c), and the expulsion events themselves do not modify the underlying flows established by the kinematics of the waiting line .

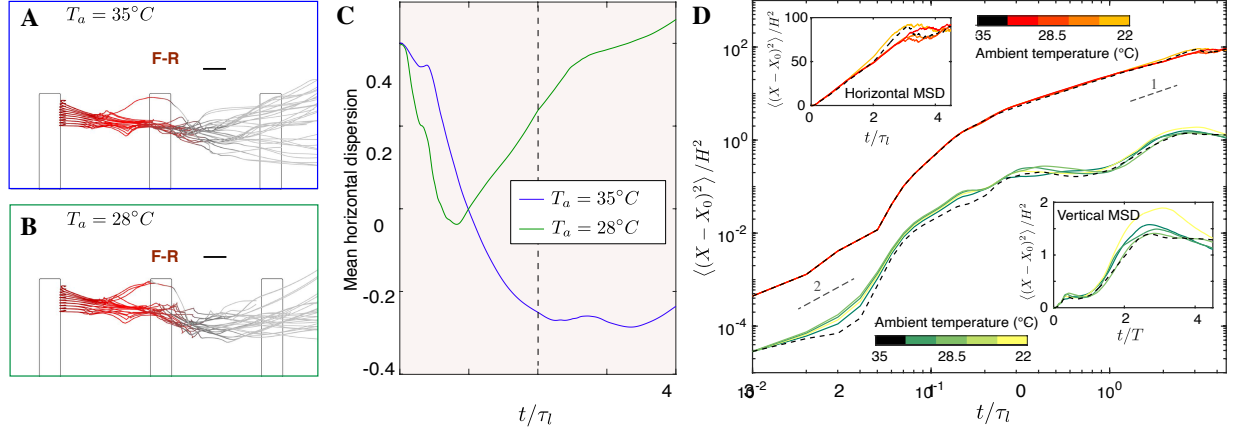


FIG. S-10. **Lagrangian trajectories and dispersion statistics from DNS for particles released on front side.** (a,b) are the trajectories of tracers for one period with different buoyancy conditions, colored with the time evolution from red to grey. Plot (a) relates to the non-buoyant case with the particles released in the front. Plot (b) relates to the buoyant case with the particles released in the front. The plot (c) is the mean horizontal (of the same direction of motion) dispersion of the Lagrangian tracers of side and rear release of both buoyant ( $T_a = 28^\circ\text{C}$ ) and non-buoyant ( $T_a = 35^\circ\text{C}$ ) case, respectively. (d) Mean squared dispersion (MSD) of the Lagrangian tracers released from the front of the cylinders for different net buoyancy conditions. The upper curves are the horizontal MSD and lower lines are that of vertical MSD of the tracers on a log scale. The insets show the same data on a linear scale.

## SUPPLEMENTARY MOVIES

Movie S1: **Non-buoyant Lagrangian tracer trajectories colored by time.** Here  $\Delta\rho/\rho = 0$  and the colors represent the normalized time  $(t/\tau_l)$  after release.

Movie S2: **Non-buoyant Lagrangian tracer trajectories colored by velocity.** Here  $\Delta\rho/\rho = 0$  and the colors represent the normalized vertical velocity  $(v/U_m)$  after release.

Movie S3: **Buoyant Lagrangian tracer trajectories colored by time.** Here  $\Delta\rho/\rho = 0.16$  and the colors represent the normalized time  $(t/\tau_l)$  after release.

Movie S4: **Buoyant Lagrangian tracer trajectories colored by velocity.** Here  $\Delta\rho/\rho = 0.16$  and the colors represent the normalized vertical velocity  $(v/U_m)$  after release..